RESEARCH ARTICLE

Key Points:
- Simulation reproduces the nighttime upward drift observed by C/NOFS
- The nighttime upward drift is caused by thermospheric dynamics related to MTM
- Longitudinal variations result from the MTM dynamics and magnetic field geometry

Correspondence to:
T.-W. Fang,
tzu-wei.fang@noaa.gov

Impact of midnight thermosphere dynamics on the equatorial ionospheric vertical drifts

T.-W. Fang[1], R. A. Akmaev[2], R. A. Stoneback[3], T. Fuller-Rowell[1], H. Wang[1], and F. Wu[1]

[1]Cooperative Institute for Research in Environmental Sciences, University of Colorado Boulder, Boulder, Colorado, USA, [2]Space Weather Prediction Center, National Oceanic and Atmospheric Administration, Boulder, Colorado, USA, [3]Physics Department, W. B. Hanson Center for Space Sciences, University of Texas at Dallas, Richardson, Texas, USA

Abstract Recent satellite and ground-based observations have revealed the existence of upward drifts in the postmidnight equatorial ionosphere (~0–3 LT). The phenomenon has not been explained by theoretical models. Simulations using the Whole Atmosphere Model coupled with the Global Ionosphere Plasmasphere model have successfully reproduced the unusual nighttime upward drifts. The simulations and observations by the Ion Velocity Meter onboard the Communications/Navigation Outage Forecasting System also reveal substantial longitudinal dependence of the drifts. Our analysis indicates that the upward drifts are driven by thermosphere dynamics associated with the midnight temperature maximum (MTM). The MTM locally reverses the typical large-scale zonal and meridional wind pattern, in turn affecting the nighttime *F* layer electrodynamics. In addition, the longitudinal variation of the drifts in different seasons depends on the magnitude and position of the MTM peak relative to the magnetic equator.

1. Introduction

Significant upward drifts, known as the prereversal enhancement (PRE), often occur in the postsunset equatorial ionosphere. PRE affects the nighttime plasma density distribution, particularly the strength of the equatorial ionization anomaly (EIA), and also contributes strongly to the formation of equatorial irregularities responsible for GPS signal scintillation and radio communication outages [*Anderson et al.*, 2004]. The morphology of ionospheric vertical drifts has been studied over the past few decades using multiple radar and satellite observations. The empirical model established by *Scherliess and Fejer* [1999] widely used in the community is capable of reproducing most of the diurnal, seasonal, and solar activity variations of the equatorial ionosphere drifts. However, examining details of the observations shown by *Scherliess and Fejer*, it appears that an upward drift feature may also be found in the nighttime period in different seasons and under different solar activity levels. The magnitude of the nighttime upward drift sometimes may even be larger than the peak daytime upward drift [*Scherliess and Fejer*, 1999; *Stoneback et al.*, 2011].

Several sets of direct and indirect measurements have recently manifested the existence of nighttime upward vertical plasma drifts. *Yizengaw et al.* [2009] reported a strong EIA in total electron content (TEC) in the postmidnight period apparently caused by the upward drifts and driven by the *F* region wind dynamo. Observations by the Ion Velocity Meter (IVM) onboard the Communications/Navigation Outage Forecasting System (C/NOFS) satellite have also revealed a large semidiurnal component in the ion drift variation at the magnetic equator, which produces significant deviations from typical climatology. Afternoon downward drifts and upward drifts around or after midnight are present in most seasons in IVM data but the magnitudes are strongest during solstice [*Stoneback et al.*, 2011]. *Stoneback et al.* suggested that the nighttime upward drift could be related to the semidiurnal tide in the ionospheric *E* region. Driving the Naval Research Laboratory SAMI3 ionosphere model with the empirical neutral wind model HWM07, results from *Huba et al.* [2010a, 2010b] found a strong dawn density depletion that is caused by a large enhancement of the postmidnight eastward electric field. Their simulation results also conclude that that zonal wind plays a significant role in the development of the postmidnight eastward electric field. *McDonald et al.* [2015] reproduced similar magnitude of the nighttime ion upward drift using the Sami3 is Also a Model of the Ionosphere (SAMI3) through specifying the neutral winds from the specified dynamics Whole Atmosphere Community Climate Model (SD-WACCM-X). Their results indicated that the nonmigrating tides play an important role. Analyzing the C/NOFS Planar Langmuir Probe (PLP) measurements, *Dao et al.* [2011] found that the plasma density irregularities were more commonly observed after midnight. *Yizengaw et al.* [2013] further showed that substantially more postmidnight plasma bubbles and scintillations were observed by the PLP in June

under quiet geomagnetic conditions. They suggested that the bubbles were generated by the increase of the growth rate of Rayleigh-Taylor (RT) instability due to the upward plasma drift. *Yokoyama et al.* [2011a, 2011b] compared the ionospheric irregularities seen in radar, GPS-TEC, and C/NOFS measurements in the postmidnight period in the Asian sector and suggested that the equatorward wind related to the midnight temperature maximum (MTM) creates conditions for the formation of the irregularities.
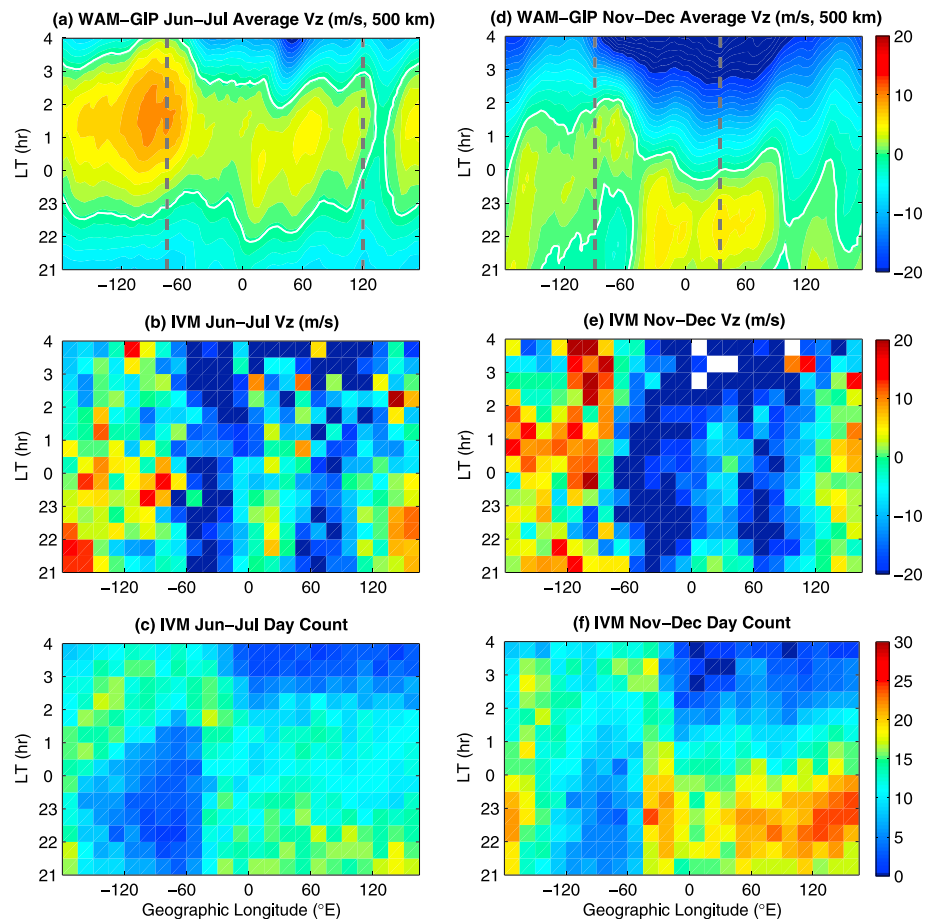
The physical process of MTM was investigated using different numerical models [*Fesen et al.*, 2002; *Colerico et al.*, 2006; *Akmaev et al.*, 2009; *Ruan et al.*, 2015]. However, possible effects of the MTM and associated dynamics on the ionosphere have not been investigated in detail or simulated by theoretical models before. The Whole Atmosphere Model (WAM) was the first comprehensive model to reproduce a robust MTM of realistic magnitude, accompanied by the midnight density maximum (MDM) and characteristic wind patterns [*Akmaev et al.*, 2009; *Akmaev et al.*, 2010]. The model results indicate that the feature may be traced down to the lower thermosphere, where it is manifested primarily in the form of an upward propagating terdiurnal tide, possibly generated in part within the thermosphere in general agreement with the nonlinear mechanism proposed by *Mayr et al.* [1979]. At higher altitudes waves of higher-order zonal wave numbers and frequencies also contribute reflecting the steepening of the temperature peak with height, also consistent with the nonlinear nature of the phenomenon. The MTM creates a significant temperature bulge around midnight at ionospheric *F* region heights and modulates the nighttime circulation. The climatology and timing of nighttime wind and temperature variations in WAM simulations have been validated with ground-based observations in equatorial Brazil and in Arecibo [*Meriwether et al.*, 2013; *Martinis et al.*, 2013]. Recently, *Hickey et al.* [2015] also confirmed the WAM prediction of MTM extending out to midlatitudes.

Since previous studies from ground-based and satellite measurements [e.g., *Li et al.*, 2011; *Yizengaw et al.*, 2013] have demonstrated higher occurrence of the postmidnight plasma density irregularities particularly in June solstices, simulations focusing on solstice periods (June–July and November–December) in 2010 are carried out. This study demonstrates that simulations using WAM coupled with the Global Ionosphere Plasmasphere (GIP) model successfully reproduce the observed nighttime equatorial upward plasma drifts. Analyzing the simulation results in two different seasons (June–July and November–December), we explain the causal mechanism of the drifts and their observed longitudinal variation confirming the strong connection between the thermosphere and ionosphere through dynamics associated with the MTM.

2. Simulation and Observation

The simulations presented in this study were carried out using WAM and GIP in a one-way coupling scheme. WAM [*Akmaev*, 2011] has been extensively validated and described in the literature over the past few years, in particular in regard to the effects on the ionosphere of tides propagating up from the lower atmosphere, for example, during sudden stratospheric warmings [*Fuller-Rowell et al.*, 2010, 2011; *Wang et al.*, 2011, 2014; *Fang et al.*, 2012, 2014]. It is a general circulation model spanning the atmosphere from the surface to an average height of about 600 km and built from an operational weather prediction model by vertical extension to the exobase. In this study, the WAM data assimilation and forecast system [*Wang et al.*, 2011, 2014] is used to produce realistic day-to-day thermospheric conditions during June–July and November–December 2010.

GIP is an upgraded ionosphere-plasmasphere-electrodynamics model [*Fang et al.*, 2009]. It utilizes a Magnetic Apex coordinate system [*Richmond*, 1995], in which a realistic global three-dimensional grid of magnetic field lines is created by tracing through the full International Geomagnetic Reference Field. The midlatitude and low-latitude portion of GIP is defined by closed flux tubes with magnetic latitude up to 60°. The high-latitude part assumes open flux tubes extend to ~10000 km. The horizontal resolution is about $1° \times 4.5°$ in latitude-longitude at midlatitude and low latitude. The altitude covers from 100 km to higher than 20,000 km. It solves continuity, momentum, and energy equations, and outputs are Ni (O^+, H^+, O_2^+, NO^+, N_2^+, N^+), Ne, Ti, Te, and Vi. O^+ and H^+ solutions include field-aligned and field perpendicular transport; the remaining ions are assumed to be in chemical equilibrium. The nighttime ionization rate in GIP is adopted from the National Center for Atmospheric Research (NCAR) Thermosphere-Ionosphere-Electrodynamics General Circulation Model (TIEGCM) and was described in *Richmond and Maute* [2013]. GIP simulations of the equatorial ionosphere have been validated through comparison with other community models and observations [*Fang et al.*, 2013a]. Using the one-way coupled WAM-GIP model, several studies focusing on understanding the impact of the lower atmosphere on the ionosphere during quiet geomagnetic conditions have been carried
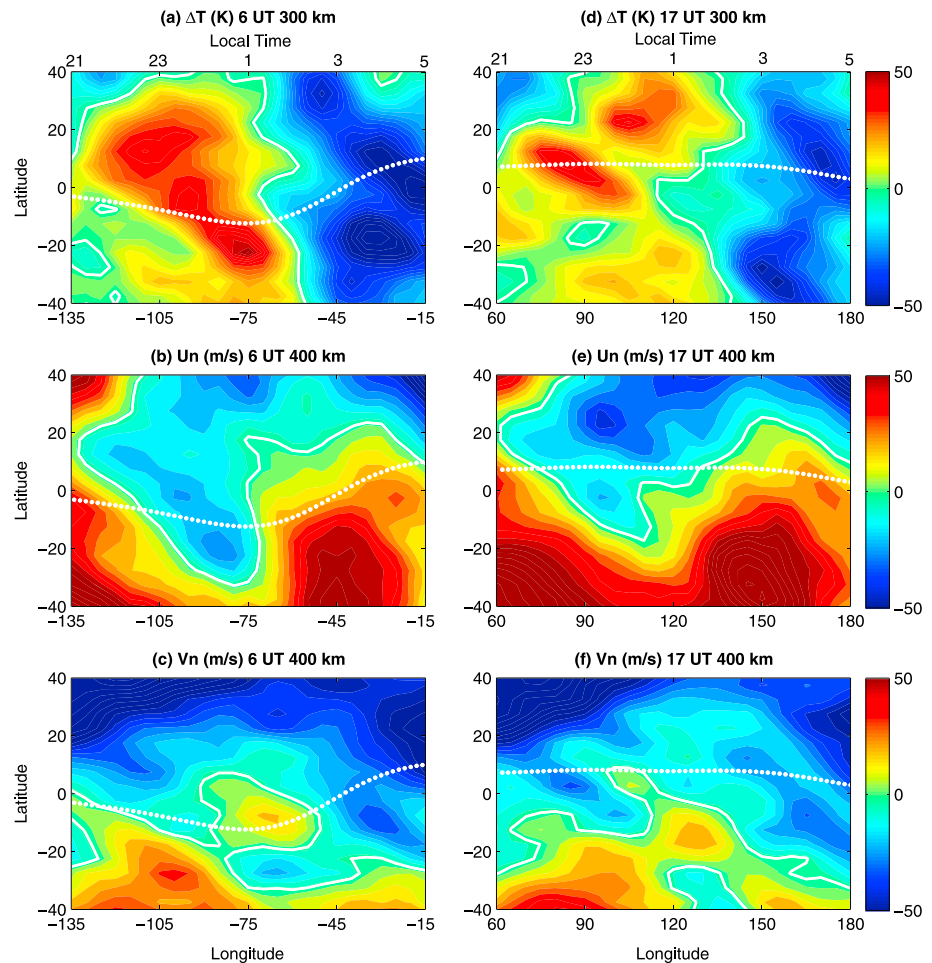
Figure 1. Ion vertical drift at magnetic equator simulated by the coupled WAM-GIP model in (a) June/July and (d) November /December periods. Black dashed lines correspond to longitude sectors shown in Figures 2, 3, and 5. Ion vertical drifts near the magnetic equator observed by the C/NOFS IVM instrument in (b) June/July and (e) November/December periods. Day count of IVM observation in the (c) June/July and (f) November/December periods.

out [*Fang et al.*, 2013b; *Fang et al.*, 2014]. To examine ionospheric electrodynamic responses to winds associated with the MTM, WAM thermospheric winds and GIP conductivities are used to drive the electrodynamic solver developed by *Richmond* [1995]. Both models were run under low solar activity (solar 10.7 cm radio flux $F_{10.7} = 70$) and geomagnetic quiet conditions ($Kp = 1$).

The observed vertical drift used in this study is obtained from the C/NOFS ion velocity meter. The ion velocity meter [*Heelis and Hanson*, 1998] is comprised of two instruments, a retarding potential analyzer (RPA) and a drift meter (DM). A retarding voltage inside the RPA may be used to control the energy of ions that have access to the detector. The variation in plasma flux as a function of energy may be used to determine basic thermal plasma parameters such as ion density, temperature, major ion composition, and the RAM velocity of plasma. The DM employs a segmented collector plate to measure the arrival angle of ions. Combined with satellite attitude and ephemeris the ion drifts relative to corotation may be extracted. For the C/NOFS satellite the geophysical boundary condition that equatorial electric fields are curl free is employed to maintain an instrument uncertainty for averaged drifts that is less than 7 m/s over the life of the mission [*Stoneback et al.*, 2012]. IVM data are publicly available through NASA CDAWeb (http://cdaweb.gsfc.nasa.gov).

IVM data have previously been used in various studies. *Araujo-Pradere et al.* [2012] demonstrated that the longitudinal distribution of ion drift from IVM has significant impact on density distributions. Seasonal and longitudinal variations between IVM drifts and Formosa Satellite Mission 3/Constellation Observing System for Meteorology, Ionosphere, and Climate electron density profiles obtained from radio occultation measurements have been shown to be consistent [*Stoneback and Heelis*, 2014]. The underlying physical connection between these two data sets has also been exploited to estimate the distribution of the ionosphere at shorter
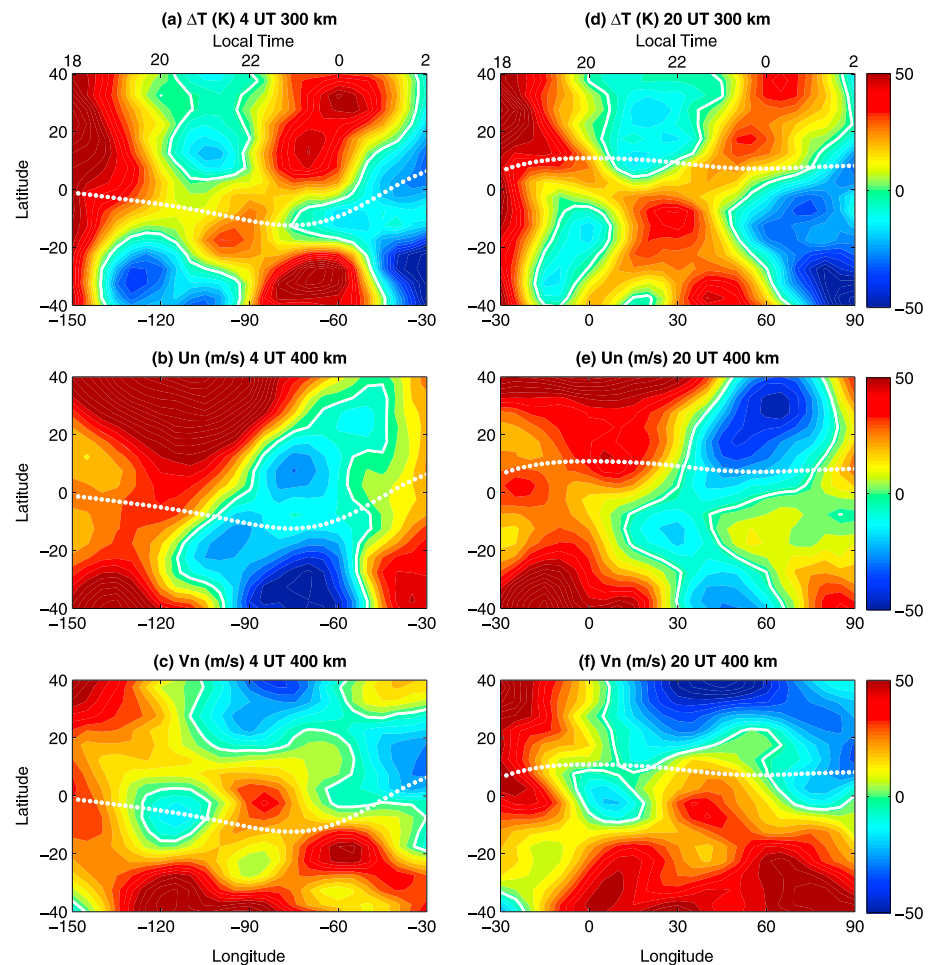
Figure 2. Temperature perturbation at 300 km (ΔT), zonal wind at 400 km (Un), and meridional wind at 400 km (Vn) simulated by the WAM at (a–c) 6 UT and (d–f) 17 UT in June–July. Positive values in zonal and meridional winds are eastward and northward, respectively. White lines are the zero contours. White dotted lines represent the location of geomagnetic equator.

timescales [*Stoneback et al.*, 2013]. The vertical ion drift has also been validated with radar measurement [*Patra et al.*, 2014]. Regions with large downward drifts from IVM measurements have been shown to coincide with large plasma decreases [*Huang et al.*, 2012]. Comparison of GRACE-derived neutral densities and IVM ion drifts shows a similar decrease in neutral densities [*Huang et al.*, 2013].

3. Results and Discussion

Figure 1 compares the 2 month average vertical ion drifts at 500 km above the magnetic equator simulated by WAM-GIP (Figures 1a and 1d) with IVM observations (Figures 1b and 1e) as a function of longitude and local time in June–July (left) and November–December (right). The white lines represent the zero contours and the black dashed lines are the longitudes selected for detailed analysis (see Figures 2–4). No significant height gradient of the nighttime vertical drift at *F* region heights is found in the simulation at these local times (LT). The locations of IVM observations are restricted to within ±12° magnetic latitude, altitudes below 550 km, and geomagnetic quiet conditions. Figures 1c and 1f show the number of days of observations in each longitude-LT bin during the two 2 month periods that are used to obtain drift velocity in Figures 1b and 1e.

In the June–July period, the simulation shows significant upward drifts with magnitudes of up to 20 m/s near and after midnight in the American sector (between 60°W and 150°W). Somewhat weaker upward vertical drifts are also observed in two other longitude sectors (0°E to 60°E and 140°E to 180°E) at about the same local time. The IVM observations confirm the existence of these upward drifts that occurs at around midnight and show similar longitudinal variation in the nighttime. The 2 month average simulated upward drifts appear to be more confined
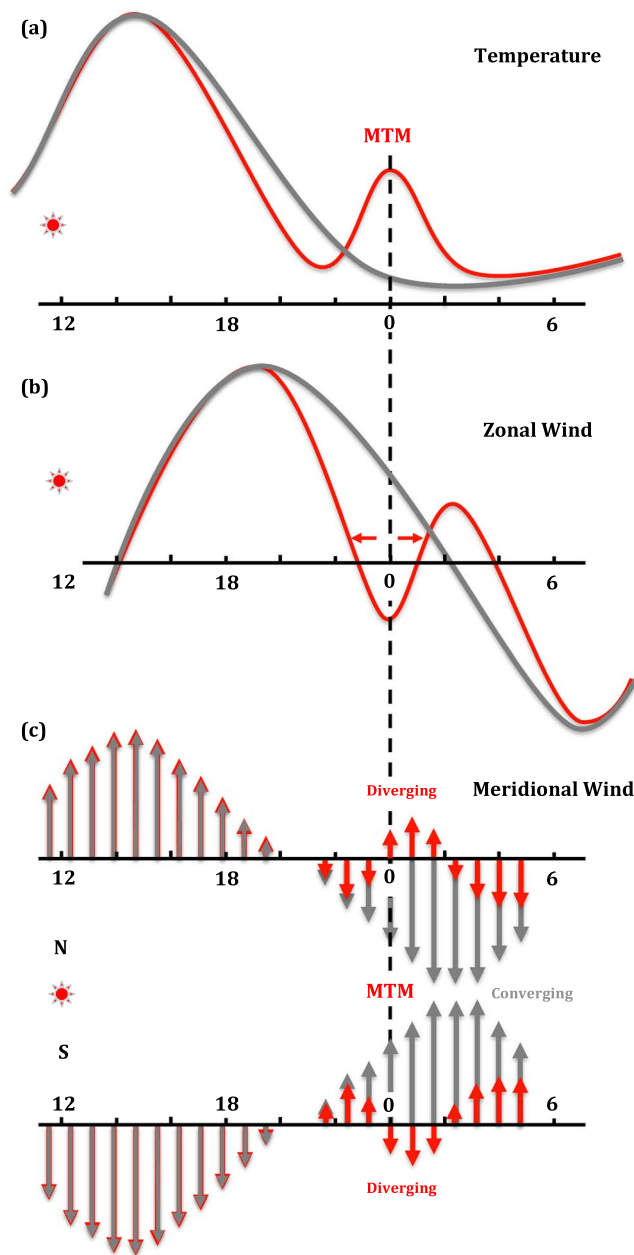
Figure 3. Same as in Figure 2 but at (a–c) 4 UT and (d–f) 20 UT during November–December.

to postmidnight, while the observed drifts occasionally show a larger velocity at some locations around midnight and the upward direction of drift extends throughout the nighttime. These large velocities in the observation occurred on some particular days (see Figure 1c) rather than throughout the whole period, which reflects the strong day-to-day variability in the ionosphere. In November–December the average simulated upward drifts in the American sector are somewhat weaker and shifted to earlier local times than in June–July. Compared to observations in this period, the magnitude of simulated upward drift is smaller in American sector (west of 60°W) but slightly larger in African sector (0° to 60°E). The observation again shows the upward direction of drift extends throughout the nighttime. For both periods, the downward drifts seen in the observations in the 0° to 60°W longitude sector are not captured in the 2 month average drift from the model. Overall, the magnitude and longitudinal distribution of simulated nighttime vertical drifts shows a better agreement with the IVM observations in June–July. The different longitudinal and LT distributions in different seasons in the simulations motivate to further investigate the physical mechanisms of the nighttime electrodynamics and its seasonal dependency.

The upward vertical drifts in both IVM observations and WAM-GIP simulations present a very different scenario from previous understanding of nighttime electrodynamic processes, i.e., primarily downward ion drift in the nighttime as represented in empirical models [e.g., *Scherliess and Fejer*, 1999]. The longitudinal distribution and seasonal dependency of the nighttime drift indicate that the upward velocity is variable and not a persistent feature occurring in the ionosphere every night, at every location and season. As is well known, the nighttime *F* region electrodynamic processes are largely controlled by the thermosphere dynamics [*Rishbeth*, 1971]. Recent studies using the NCAR TIEGCM coupled with GIP have revealed more details of *F* region dynamo during the postsunset period [*Richmond et al.*, 2015; *Richmond and Fang*, 2015]. The simulations confirmed that the PRE is driven primarily by an increasing eastward zonal wind (acceleration) forced by the diurnally varying zonal pressure
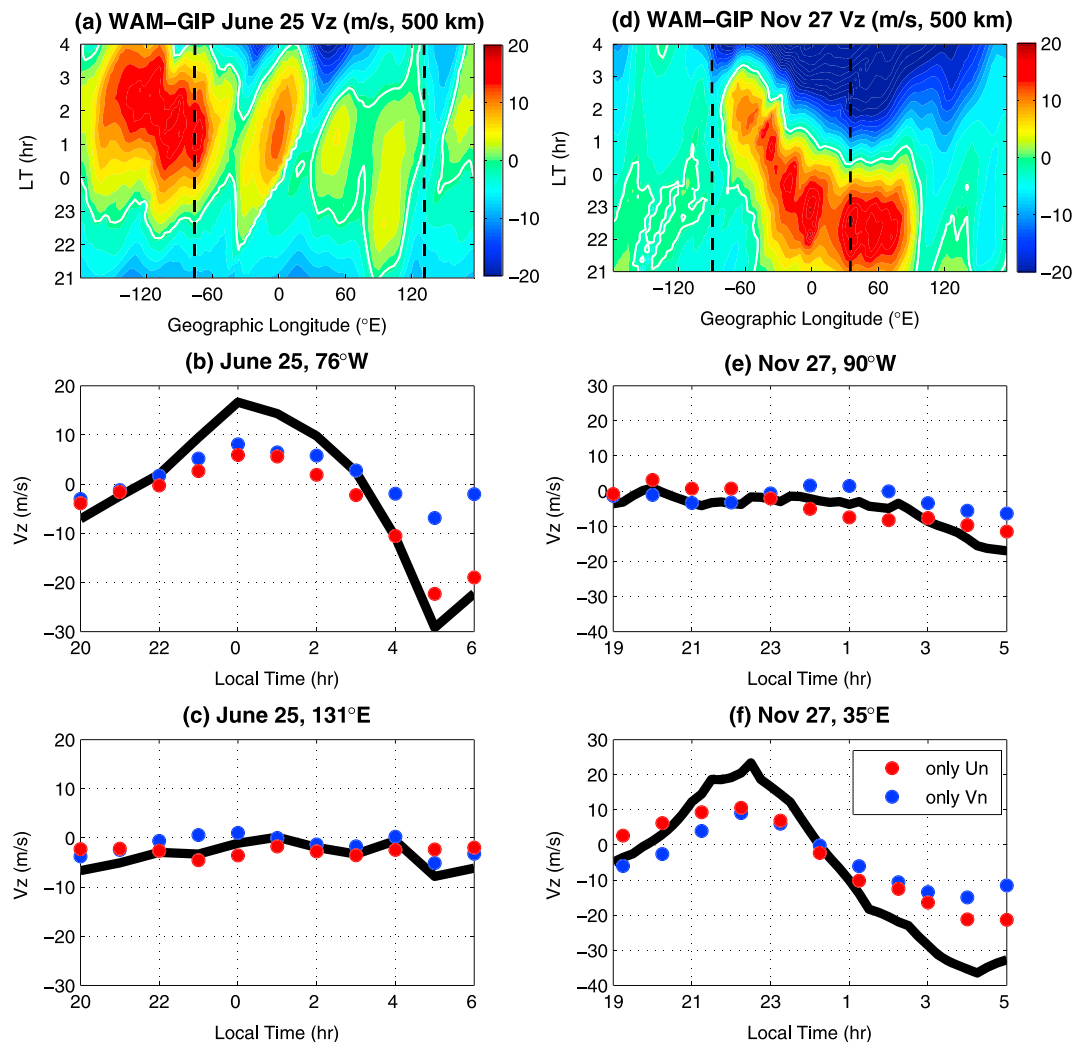
Figure 4. Schematic plot of local time variations of neutral temperature, zonal wind, and meridional wind with MTM (red lines and arrows) and without MTM (gray lines and arrows).

gradient force when the *E* region conductivity is diminished after sunset. The eastward zonal wind at dusk is driven by the large-scale solar-driven dayside temperature and pressure bulge. The zonal pressure gradients are therefore fairly uniform in latitude and altitude. Through different numerical experiments, these studies also found that the postsunset *F* region zonal winds at latitudes that encompass the EIA are the main driver of the eastward plasma convection, which increases into the evening and connects to the upward/poleward convection that constitutes the PRE. During the nighttime period, local thermosphere dynamics features associated with the temperature bulge in MTM also lead to a pressure gradient driving zonal winds similar to those driving the PRE but the impact is predominately on the ionospheric *F* region height. Unlike the day to night circulation that drives the large-scale poleward meridional wind, the MTM dynamics creates a rather localized impact on the meridional wind [*Akmaev et al.*, 2009].

Figure 2 shows the June–July average of temperature deviation at 300 km from the nighttime longitude mean (e.g., between 15°W and 135°W in Figure 2a) and of total zonal (positive eastward) and meridional (positive northward) winds at 400 km simulated by WAM at 6 UT (a–c) and 17 UT (d–f). These UT instances correspond to 1 LT at longitudes of 75°W and 120°E, approximately where the simulations show a maximum and a minimum in the upward nighttime drifts (Figure 1a), respectively. In November–December (Figure 3) the same parameters are presented at 4 UT (a–c) and 20 UT (d–f), these UT instances corresponding to 22 LT at longitude of 30°E and 90°W where the simulations also show a maximum and a minimum in the nighttime drift (Figure 1d). The white solid lines represent the zero contour and the dotted white lines show the magnetic equator. Using the 2 month averaged winds from the June–July and November–December periods to drive the GIP, the results do show similar magnitudes and longitude-LT variations of the nighttime drifts as those in Figures 1a and 1d (not shown here). The temperature deviation (Figures 1a and 1d) generally follows the familiar MTM V-shaped distribution in latitude-longitude indicating that the maximum occurs first in the equatorial region and at later local times away from the equator [*Akmaev et al.*, 2009; *Martinis et al.*, 2013; *Hickey et al.*, 2015]. The magnitude of the peak and smaller-scale variations within the feature are also clearly longitude dependent. The temperature maximum in the underlying layers, say at 300 km (Figures 2a and 2d and 3a and 3d), raises the pressure at heights above that level via hydrostatic balance, resulting in a local

Figure 5. Ion vertical drifts at magnetic equator simulated by the coupled WAM-GIP model on (a) 25 June and (d) 27 November. Simulated nighttime equatorial vertical drift (black lines) (b and c) on 25 June and (e and f) on 27 November at different longitudes. Red and blue dots are simulation results with only zonal wind (only Un) and only meridional wind (only Vn), respectively.

pressure bulge [*Akmaev et al.*, 2010]. Just as the day-night pressure gradient drives the eastward gradient of zonal wind across the evening terminator resulting in PRE [e.g., *Richmond et al.*, 2015], the horizontal pressure gradients on the pressure bulge edge, say at 400 km, drive divergent winds away from the bulge (Figures 2b, 2c, 2e, and 2f and 3b, 3c, 3e, and 3f). The total wind magnitude and direction is then determined by superposition of the local divergent MTM-related structures and the prevailing large-scale seasonal and diurnal patterns.

Analysis of thermosphere dynamics in the different longitude sectors presented in Figures 2 and 3 enables deeper insight into the mechanism of nighttime upward drifts. The strong postmidnight upward drift in the American sector near 75°W is clearly associated with eastward acceleration (increasing magnitude) of the zonal wind at low latitudes (Figure 2b) on the eastward edge of the pressure bulge driven by the underlying temperature maximum at lower altitudes (Figure 2a). The eastward acceleration of the zonal wind along the magnetic equator results in an ion convection pattern similar to the conditions during the PRE and creates an upward ion drift [*Rishbeth*, 1971; *Richmond et al.*, 2015]. The meridional winds are more structured and more difficult to interpret. The midnight temperature feature in Figure 2a has a local maximum close to the magnetic equator (75°W, 20°S) that drives a localized divergence in the meridional wind, fairly symmetrically with respect to the magnetic equator, i.e., poleward wind on either side of the magnetic equator, in the same LT-longitude sector (Figure 2c). In this case, the meridional wind would contribute equally to the upward drift maximum (shown later in Figure 5b). The symmetric poleward meridional winds on either side of the magnetic equator drive

the westward Pedersen current setting the eastward polarization electric field and contributing to the upward plasma drift [*Rishbeth*, 1971]. In the longitude sector centered at 120°E the temperature maximum at 300 km (Figure 2d) also creates a pressure bulge and similar divergent wind structures (Figures 2e and 2f) in the same local time period at the low-latitude region. However, the upward drift is very weak at this longitude (Figure 1a) apparently because the divergent wind patterns are formed on one side of the magnetic equator and cannot contribute efficiently to the upward postmidnight drift (see also Figure 5c).

Even though the temperature peak extends to midlatitudes (Figures 2a and 2d), it is not unexpected that the localized divergent structure in the total meridional wind only form south of the geographic equator centering approximately at 20°S (Figures 2c and 2f) during this season. In the absence of MTM the background meridional wind structure would be dominated by superposition of a diurnal day-to-night flow and a weaker seasonal summer-to-winter flow with converging and therefore weak winds near the antisubsolar latitude. On this background, the divergent winds flowing away from the MTM pressure bulge are the main component of the total meridional wind at this latitude. Besides the interplay between the shape and location of the MTM-related local structures in the wind components relative to the magnetic equator, clearly the magnitude of the temperature peak also plays a role. For example, the 2 month average temperature deviation at 6 UT reaches a maximum of about 53 K near latitude 20°S at 1 LT (Figure 2a), while at 17 UT it is much weaker in the other longitude sector (Figure 2d).

The longitude sectors shown in Figure 3 correspond to weak (a–c) and moderate (d–f) nighttime upward drifts LT in November–December (Figure 1d). Note that the temperature perturbations at 300 km (Figures 3a and 3d) again exhibit a robust MTM feature extending from the geographic equator at about 22 LT to midlatitudes at later times. In the longitude sector centered at 90°W (Figure 3b), the coherent and symmetric area of eastward acceleration of the total zonal wind at either side of magnetic equator does occur after 1 LT when a weak upward drift is obtained (Figure 1d). However, at 22 LT the total zonal wind above the MTM is actually slowing down and reversing to westward, apparently driven by the weakening of the large-scale day-night pressure gradient. There is no symmetric divergent feature in the total meridional wind at EIA region (Figure 3c) throughout the night in this longitude sector and the meridional wind does not contribute to the upward drift (Figure 1d). The longitude sector centered at 30°E at 20 UT (Figures 3d–3f) presents yet another interesting scenario. The MTM V-shaped temperature deviation centered on the geomagnetic equator takes place just east of 30°E at about 23 LT; however, the corresponding divergent structures in total winds occur beyond the EIA region and are not able to produce the upward drift. There is also an evening (about 20 LT and at around longitude 0°) local temperature maximum on the geomagnetic equator (Figure 3d), which is connected to the main feature of MTM at later hours. Such localized postsunset temperature enhancements preceding the main MTM by several hours have been observed at low latitudes at solstice [e.g., *Herrero and Spencer*, 1982; *Faivre et al.*, 2006] and simulated by WAM in December [e.g., *Akmaev et al.*, 2009]. The localized temperature enhancement also exhibits strong day-to-day variation in our simulation and its magnitude can reach more than 70 K in some days during the November–December period. This temperature maximum does generate a weak eastward gradient in zonal wind and a divergence of meridional wind symmetric with respect to the magnetic equator at about 21 LT (Figures 3e and 3f). However, since the magnitude of meridional wind is close to zero at low latitudes, the enhanced upward drifts at this local time sector are dominated by the zonal wind (Figure 1d).

To summarize the characteristics of *F* region wind associated with the MTM dynamics, a schematic plot is presented in Figure 4. The local time variation of temperature (a), zonal wind (b), and meridional wind (c) in the low-latitude region are shown in the figure. The grey lines and arrows represent the regular diurnal variation of thermosphere caused by the solar heating. The red lines and arrows are for the thermospheric conditions under the existence of MTM. For the zonal wind, the curve stands for eastward and westward wind above and below the axis, respectively. For the meridional wind, the upper and lower parts are the northern and southern hemisphere, respectively. The location of the sun demonstrates the approximate LT for the subsolar point. As shown in the plot, the regular diurnal variation of temperature tends to peak at round 14 LT. The increased temperature creates strong horizontal pressure gradient to increase the eastward zonal wind (maximizes at dusk) and the poleward meridional wind (peaks at round 14 LT). In the nighttime, the temperature decreases, the zonal wind turns westward, and the meridional wind blows toward equator. When the MTM is present, the temperature increases near the midnight period, which reduces the eastward zonal wind at premidnight and enhances the eastward zonal wind at postmidnight. The increased temperature also reverses the meridional wind from its typical equatorward direction to poleward direction in the nighttime. Note that the amplitudes of eastward zonal wind and poleward meridional wind association with the MTM are much

weaker in the nighttime compared to those in the daytime since the temperature enhancement cause by the MTM heating is smaller and rather localized. The increased zonal gradient of zonal wind caused by the MTM provides a similar condition as those during the PRE at 19 LT to generate an upward ion drift motion. Notice that between 0 and 1 LT, the zonal wind is increasing in the eastward direction, similar to the 18 to 19 LT dusk period. Different from the PRE, the divergence feature of meridional wind after midnight does play an important role on the formation of the upward drift through the *F* region dynamo.

To evaluate the relative contribution of the zonal and meridional wind components to the upward drifts and their longitudinal structure in both seasons (Figure 1), a series of sensitivity experiments was conducted, similar to those presented before [e.g., *Fang et al.*, 2014; *Richmond and Fang*, 2015; *Richmond et al.*, 2015]. In these experiments, the GIP is run with only zonal wind (only Un) or only meridional wind (only Vn) from the WAM for one-time step to distinguish the wind impact on the electrodynamics. The electric fields calculated from this dynamo test do not feedback to the ionospheric calculation. The field line-integrated conductivities used for the baseline, only Un, and only Vn calculations are the same at a given time. Days with similar longitudinal variations as those in the 2 month averaged drifts (Figures 1a and 1d) were chosen to demonstrate the impact of zonal and meridional wind. For example, Figure 5a shows the longitudinal variation of the nighttime vertical drift at 500 km above the magnetic equator on a typical day, 25 June 2010. The differences between Figures 5a and 1a demonstrate strong day-to-day variability of the simulated vertical ion drift, which has to be taken into account when comparing to the observations (Figure 1b) covering only a few days (Figure 1c) during this period. The vertical drifts at longitudes 76°W and 131°E as a function of local time on this particular day are also shown (Figures 5b and 5c, black line). The two longitudes approximately correspond to the locations with strong and weak upward drifts on 25 June (Figure 5a) as well as in the 2 month average (Figure 1a). In the American sector (Figure 5b) the upward nighttime drift maximizes at ~17 ms^{-1} near midnight LT on this particular day followed by a strong downward velocity in the early morning (black line). The vertical drifts calculated by the dynamo module with only zonal (red dots) or only meridional (blue dots) wind component applied are also shown at each local time. It is clearly seen that the local MTM-related structures in both the zonal and meridional wind components (Figures 2b and 2c) contribute equally to the upward nighttime drift in this longitude sector. This is contrasted by a very weak upward tendency in the drift at 131°E near 1 LT (Figure 5c). Neither wind component contributes strongly at this location and local time (see also Figures 2e and 2f). There is no coherent eastward acceleration of zonal wind encompassing the EIA on both sides of the magnetic equator as required, for example, for the PRE [*Richmond et al.*, 2015]. A divergent meridional wind structure is entirely confined south of the magnetic equator making it inefficient in generating an eastward polarization electric field, and the overall magnitude of the underlying MTM peak is weaker than in the American sector.

Similar dynamo tests are carried out on another day, 27 November 2010. Figure 5d shows the local time and longitudinal distribution of simulated vertical drift at 500 km. Local time variations of nighttime drift at longitudes 90°W and 35°E of this particular day are also shown (Figures 5e and 5f, black line). The two longitudes approximately correspond to the locations with weak and strong upward drifts on 27 November (Figure 5d) as well as in the 2 month average (Figure 5d) indicating the day-to-day variability. The peak vertical drift on this day shows much larger magnitude compared to the 2 month average (Figure 5d). At 35°E, the nighttime upward drift peaks at around 22.5 LT, and the simulation results suggest again that both wind components contribute approximately equally. The zonal gradient of zonal wind is strong and consistent in the whole EIA region (Figure 3e) resulting in an upward drift after about 20 LT. The divergence of meridional wind after 21 LT (Figure 3f) also contributes driving an eastward polarization electric field, as described earlier. The upward drift and the distribution of winds that occur before midnight are strongly controlled by the dynamics associated with the local temperature maximum (Figure 3d). The spatial distribution of winds at 90°W (Figures 3b and 3c) does not show the large eastward gradient of zonal wind or the divergence of meridional wind, and no upward nighttime drift is found at this longitude. Using the 2 month averaged wind shown in Figures 2 and 3 for the sensitivity tests, similar conclusions can be drawn (not shown here).

4. Conclusions

Recent direct and indirect observations with multiple satellite and ground-based instruments suggest the existence of substantial upward plasma drifts and associated plasma instabilities in the quiet nighttime equatorial ionosphere, particularly around June solstice. A coupled whole atmosphere and ionosphere/plasmasphere model was used to simulate the global nighttime *F* region electrodynamics in

June–July and November–December 2010. The WAM-GIP model simulations successfully reproduced the magnitude, timing, and longitudinal variation of the nighttime upward vertical drifts in good agreement with the IVM observations from C/NOFS during the June–July period. Comparing the simulation results in the two seasons, the upward drifts tend to occur at locations where the magnetic equator goes through the winter hemisphere and the occurrence time of peak upward drift happens at earlier LT in November–December.

The simulation results confirm that the nighttime upward vertical drifts in the equatorial ionosphere are driven by local dynamics associated with the thermospheric MTM and similar local features. Furthermore, sensitivity studies indicate that depending on longitude both the zonal and meridional wind component may contribute to the electrodynamic processes. A coherent eastward acceleration of the zonal wind on both sides of the magnetic equator on the eastward flank of the pressure bulge associated with the MTM drives the poleward-upward plasma convection similar to that occurring during the PRE. Additionally, poleward structures in the total meridional wind may drive an eastward electric field and upward plasma drift if they happen to straddle the magnetic equator as in the American sector in June–July.

Overall, the magnitude, timing, and longitudinal variation of the upward nighttime drifts is determined by the interplay between the shape and location of the MTM and related local structures in temperature and wind components relative to the magnetic equator as well as by the magnitude of the temperature peak. It has been previously suggested that the MTM itself is possibly driven by nonlinear interactions of tides propagating from the lower atmosphere with a diurnally varying ion drag. Future modeling studies with two-way coupled whole atmosphere-ionosphere models will shed more light on relative contributions of neutral-ion and ion-neutral interactions on the nighttime dynamics and electrodynamics of the equatorial thermosphere-ionosphere system. Both observational and modeling studies of seasonal, solar activity, and longitudinal variations will be of particular interest and importance.

References

Akmaev, R. A. (2011), Whole atmosphere modeling: Connecting terrestrial and space weather, *Rev. Geophys.*, *49*, RG4004, doi:10.1029/2011RG000364.

Akmaev, R. A., F. Wu, T. J. Fuller-Rowell, and H. Wang (2009), Midnight temperature maximum (MTM) in Whole Atmosphere Model (WAM) simulations, *Geophys. Res. Lett.*, *36*, L07108, doi:10.1029/2009GL037759.

Akmaev, R. A., F. Wu, T. J. Fuller-Rowell, H. Wang, and M. D. Iredell (2010), Midnight density and temperature maxima, and thermospheric dynamics in Whole Atmosphere Model simulations, *J. Geophys. Res.*, *115*, A08326, doi:10.1029/2010JA015651.

Anderson, D. N., B. Reinisch, C. Valladares, J. Chau, and O. Veliz (2004), Forecasting the occurrence of ionospheric scintillation activity in the equatorial ionosphere on a day-to-day basis, *J. Atmos. Sol. Terr. Phys.*, *66*, 1567–1572.

Araujo-Pradere, E., T.-W. Fang, D. N. Anderson, M. Fedrizzi, and R. Stoneback (2012), Modeling the daytime, equatorial ionospheric ion densities associated with the observed, four-cell longitude patterns in $E \times B$ drift velocities, *Radio Sci.*, *47*, RS0L12, doi:10.1029/2011RS004930.

Colerico, M. J., M. Mendillo, C. G. Fesen, and J. Meriwether (2006), Comparative investigations of equatorial electrodynamics and low-to-mid latitude coupling of the thermosphere-ionosphere system, *Ann. Geophys.*, *24*, 503–513, doi:10.5194/angeo-24-503-2006.

Dao, E., M. C. Kelley, P. Roddy, J. Retterer, J. O. Ballenthin, O. de La Beaujardiere, and Y.-J. Su (2011), Longitudinal and seasonal dependence of nighttime equatorial plasma density irregularities during solar minimum detected on the C/NOFS satellite, *Geophys. Res. Lett.*, *38*, L10104, doi:10.1029/2011GL047046.

Faivre, M., J. W. Meriwether, C. G. Fesen, and M. A. Biondi (2006), Climatology of the midnight temperature maximum phenomenon at Arequipa, Peru, *J. Geophys. Res.*, *111*, A06302, doi:10.1029/2005JA011321.

Fang, T.-W., H. Kil, G. Millward, A. D. Richmond, J.-Y. Liu, and S.-J. Oh (2009), Causal link of the wave-4 structures in plasma density and vertical plasma drift in the low-latitude ionosphere, *J. Geophys. Res.*, *114*, A10315, doi:10.1029/2009JA014460.

Fang, T.-W., T. Fuller-Rowell, R. Akmaev, F. Wu, H. Wang, and D. Anderson (2012), Longitudinal variation of ionospheric vertical drifts during the 2009 sudden stratospheric warming, *J. Geophys. Res.*, *117*, A03324, doi:10.1029/2011JA017348.

Fang, T.-W., et al. (2013a), Comparative studies of theoretical models in the equatorial ionosphere, in *Modeling the Ionosphere-Thermosphere*, *Geophys. Monogr. Ser.*, vol. 201, edited by J. D. Huba, pp. 360, AGU, Washington, D. C.

Fang, T.-W., R. Akmaev, T. Fuller-Rowell, F. Wu, N. Maruyama, and G. Millward (2013b), Longitudinal and day-to-day variability in the ionosphere from lower atmosphere tidal forcing, *Geophys. Res. Lett.*, *40*, 2523–2528, doi:10.1002/grl.50550.

Fang, T.-W., T. Fuller-Rowell, H. Wang, R. Akmaev, and F. Wu (2014), Ionospheric response to sudden stratospheric warming events at low and high solar activity, *J. Geophys. Res. Space Physics*, *119*, 7858–7869, doi:10.1002/2014JA020142.

Fesen, C. G., D. L. Hysell, J. M. Meriwether, M. Mendillo, B. G. Fejer, R. G. Roble, B. W. Reinish, and M. A. Giondi (2002), Modeling the low-latitude thermosphere and ionosphere, *J. Atmos. Sol. Terr. Phys.*, *64*, 1337–1349, doi:10.1016/S1364-6826(02)00098-6.

Fuller-Rowell, T., F. Wu, R. Akmaev, T.-W. Fang, and E. Araujo-Pradere (2010), A whole atmosphere model simulation of the impact of a sudden stratospheric warming on thermosphere dynamics and electrodynamics, *J. Geophys. Res.*, *115*, A00G08, doi:10.1029/2010JA015524.

Fuller-Rowell, T., H. Wang, R. Akmaev, F. Wu, T.-W. Fang, M. Iredell, and A. Richmond (2011), Forecasting the dynamic and electrodynamic response to the January 2009 sudden stratospheric warming, *Geophys. Res. Lett.*, *38*, L13102, doi:10.1029/2011GL047732.

Heelis, R. A., and W. Hanson (1998), Measurements of thermal ion drift velocity and temperature using planar sensors, in *Measurement Techniques in Space Plasmas: Particles*, vol. 102, edited by R. F. Pfaff et al., pp. 61–71, AGU, Washington, D. C.

Herrero, F. A., and N. W. Spencer (1982), On the horizontal distribution of the equatorial thermospheric midnight temperature maximum and its seasonal variation, *Geophys. Res. Lett.*, *9*, 1179–1182, doi:10.1029/GL009i010p01179.

Hickey, D. A., C. R. Martinis, P. J. Erickson, L. P. Goncharenko, J. W. Meriwether, R. Mesquita, W. L. Oliver, and A. Wright (2015), New radar observations of temporal and spatial dynamics of the midnight temperature maximum at low latitude and midlatitude, *J. Geophys. Res. Space Physics*, *119*, 10,499–10,506, doi:10.1002/2014JA020719.

Huang, C. Y., S. H. Delay, P. A. Roddy, E. K. Sutton, and R. Stoneback (2012), Longitudinal structures in the equatorial ionosphere during deep solar minimum, *J. Atmos. Sol. Terr. Phys.*, *90–91*, 156–163, doi:10.1016/j.jastp.2012.04.012.

Huang, C. Y., P. A. Roddy, E. K. Sutton, R. Stoneback, R. F. Pfaff, L. C. Gentile, and S. H. Delay (2013), Ion-neutral coupling during deep solar minimum, *J. Atmos. Sol. Terr. Phys.*, *103*, 138–146, doi:10.1016/j.jastp.2012.11.009.

Huba, J. D., G. Joyce, J. Krall, C. L. Siefring, and P. A. Bernhardt (2010a), Self-consistent modeling of equatorial dawn density depletions with SAMI3, *Geophys. Res. Lett.*, *37*, L03104, doi:10.1029/2009GL041492.

Huba, J. D., G. Joyce, J. Krall, C. L. Siefring, and P. A. Bernhardt (2010b), Correction to "Self-consistent modeling of equatorial dawn density depletions with SAMI3," *Geophys. Res. Lett.*, *37*, L20104, doi:10.1029/2010GL045004.

Li, G., B. Ning, M. A. Abdu, X. Yue, L. Liu, W. Wan, and L. Hu (2011), On the occurrence of postmidnight equatorial *F* region irregularities during the June solstice, *J. Geophys. Res.*, *116*, A04318, doi:10.1029/2010JA016056.

Martinis, C., D. Hickey, W. Oliver, N. Aponte, C. G. M. Brum, R. Akmaev, A. Wright, and C. Miller (2013), The midnight temperature maximum from Arecibo incoherent scatter radar ion temperature measurements, *J. Atmos. Sol. Terr. Phys.*, *103*, 129–137, doi:10.1016/j.jastp.2013.04.014.

Mayr, H. G., I. Harris, N. W. Spencer, A. E. Hedin, L. E. Wharton, H. S. Porter, J. C. G. Walker, and H. C. Carlson Jr. (1979), Tides and the midnight temperature anomaly in the thermosphere, *Geophys. Res. Lett.*, *6*, 447–450, doi:10.1029/GL006i006p00447.

McDonald, S. E., F. Sassi, and A. J. Mannucci (2015), SAMI3/SD-WACCM-X simulations of ionospheric variability during northern winter 2009, *Space Weather*, *13*, 568–584, doi:10.1002/2015SW001223.

Meriwether, J. W., J. J. Makela, D. J. Fisher, R. A. Buriti, A. F. Medeiros, R. A. Akmaev, T. J. Fuller-Rowell, and F. Wu (2013), Comparisons of thermospheric wind and temperature measurements in equatorial Brazil to Whole Atmosphere Model Predictions, *J. Atmos. Sol. Terr. Phys.*, *103*, 103–112, doi:10.1016/j.jastp.2013.04.002.

Patra, A. K., P. P. Chaitanya, Y. Otsuka, T. Yokoyama, M. Yamamoto, R. Stoneback, and R. A. Heelis (2014), Vertical ExB drifts from radar and C/NOFS observations in the Indian and Indonesian sectors: Consistency of observations and model, *J. Geophys. Res. Space Physics*, *119*, 3777–3788, doi:10.1002/2013JA019732.

Richmond, A. D. (1995), Ionospheric electrodynamics using magnetic apex coordinates, *J. Geomagn. Geoelectr.*, *47*, 191–212, doi:10.5636/jgg.47.191.

Richmond, A. D., and A. Maute (2013), Ionospheric electrodynamics modeling, in *Modeling the Ionosphere-Thermosphere System*, *Geophys. Monogr. Ser.*, vol. 201, edited by J. Huba, R. Schunk, and G. Khazanov, pp. 57–71, AGU, Washington, D. C., doi:10.1029/2012GM001331. (also published online in 2014 by John Wiley, Chichester, U. K. doi:10.1002/9781118704417.ch6).

Richmond, A. D., and T.-W. Fang (2015), Electrodynamics of the equatorial evening ionosphere: 2. Conductivity influences on convection, current, and electrodynamic energy flow, *J. Geophys. Res. Space Physics*, *120*, 2133–2147, doi:10.1002/2014JA020935.

Richmond, A. D., T.-W. Fang, and A. Maute (2015), Electrodynamics of the equatorial evening ionosphere: 1. Importance of winds in different regions, *J. Geophys. Res. Space Physics*, *120*, 2118–2132, doi:10.1002/2014JA020934.

Rishbeth, H. (1971), The *F*-layer dynamo, *Planet. Space Sci.*, *19*, 263–267, doi:10.1016/0032-0633(71)90205-4.

Ruan, H., J. Du, M. Cook, W. Wang, J. Yue, Q. Gan, X. Dou, and J. Lei (2015), A numerical study of the effects of migrating tides on thermosphere midnight density maximum, *J. Geophys. Res. Space Physics*, *120*, 6766–6778, doi:10.1002/2015JA021190.

Scherliess, L., and B. G. Fejer (1999), Radar and satellite global equatorial *F* region vertical drift model, *J. Geophys. Res.*, *104*(A4), 6829–6842, doi:10.1029/1999JA900025.

Stoneback, R. A., and R. A. Heelis (2014), Identifying equatorial ionospheric irregularities using in situ ion drifts, *Ann. Geophys.*, *32*, 421–429, doi:10.5194/angeo-32-421-2014.

Stoneback, R. A., R. A. Heelis, A. G. Burrell, W. R. Coley, B. G. Fejer, and E. Pacheco (2011), Observations of quiet time vertical ion drift in the equatorial ionosphere during the solar minimum period of 2009, *J. Geophys. Res.*, *116*, A12327, doi:10.1029/2011JA016712.

Stoneback, R., R. L. Davidson, and R. A. Heelis (2012), Ion drift meter calibration and photoemission correction for the C/NOFS satellite, *J. Geophys. Res.*, *117*, A08323, doi:10.1029/2012JA017636.

Stoneback, R., N. K. Malakar, D. J. Lary, and R. A. Heelis (2013), Specifying the equatorial ionosphere using CINDI on C/NOFS, COSMIC, and data interpolating empirical orthogonal functions, *J. Geophys. Res. Space Physics*, *118*, 6706–6722, doi:10.1002/jgra.50596.

Wang, H., T. J. Fuller-Rowell, R. A. Akmaev, M. Hu, D. T. Kleist, and M. Iredell (2011), First simulations with a whole atmosphere data assimilation and forecast system: The January 2009 major sudden stratospheric warming, *J. Geophys. Res.*, *116*, A12321, doi:10.1029/2011JA017081.

Wang, H., R. A. Akmaev, T.-W. Fang, T. J. Fuller-Rowell, F. Wu, N. Maruyama, and M. D. Iredell (2014), First forecast of a sudden stratospheric warming with a coupled whole-atmosphere/ionosphere model IDEA, *J. Geophys. Res. Space Physics*, *119*, 2079–2089, doi:10.1002/2013JA019481.

Yizengaw, E., M. B. Moldwin, Y. Sahai, and R. de Jesus (2009), Strong postmidnight equatorial ionospheric anomaly observations during magnetically quiet periods, *J. Geophys. Res.*, *114*, A12308, doi:10.1029/2009JA014603.

Yizengaw, E., J. Retterer, E. E. Pacheco, P. Roddy, K. Groves, R. Caton, and P. Baki (2013), Postmidnight bubbles and scintillations in the quiet-time June solstice, *Geophys. Res. Lett.*, *40*, 5592–5597, doi:10.1002/2013GL058307.

Yokoyama, T., M. Yamamoto, Y. Otsuka, M. Nishioka, T. Tsugawa, S. Watanabe, and R. F. Pfaff (2011a), On postmidnight low-latitude ionospheric irregularities during solar minimum: 1. Equatorial Atmosphere Radar and GPS-TEC observations in Indonesia, *J. Geophys. Res.*, *116*, A11325, doi:10.1029/2011JA016797.

Yokoyama, T., R. F. Pfaff, P. A. Roddy, M. Yamamoto, and Y. Otsuka (2011b), On postmidnight low-latitude ionospheric irregularities during solar minimum: 2. C/NOFS observations and comparisons with the Equatorial Atmosphere Radar, *J. Geophys. Res.*, *116*, A11326, doi:10.1029/2011JA016798.